Anisotropic reversible mixed-state properties of superconducting carbon-doped Mg(B$_{1-x}$C$_x$)$_2$ single crystals

C. Krutzler,[1,*] M. Zehetmayer,[1] M. Eisterer,[1] H. W. Weber,[1] N. D. Zhigadlo,[2] J. Karpinski,[2] and A. Wisniewski[3]

[1]*Atomic Institute of the Austrian Universities, 1020 Vienna, Austria*
[2]*Solid State Physics Laboratory, ETH, 8093 Zürich, Switzerland*
[3]*Institute of Physics, Polish Academy of Sciences, 02-668 Warsaw, Poland*

We report on magnetic and torque measurements on carbon-doped Mg(B$_{1-x}$C$_x$)$_2$ single crystals with x =0.038, 0.066, and 0.095. One-band Ginzburg Landau (GL) and London theories are applied to derive the reversible parameters: i.e., the upper critical fields H_{c2}, the coherence lengths ξ, the penetration depths λ, the anisotropy γ, the lower critical fields H_{c1}, and the GL parameter κ for fields parallel and perpendicular to the crystallographic ab plane. Due to the persistence of two-band superconductivity in the investigated doping range, these parameters turn out to depend not only on temperature, as in the case of one-band superconductors, but also on field. Therefore, the evaluation was carried out separately for two field regions: first for fields near H_{c1} and second close to H_{c2}. In general, the upper critical field increases and the anisotropy decreases upon carbon doping. All further reversible parameters are significantly modified as well. These modifications are compared for single crystals with different carbon concentration.

I. INTRODUCTION

Tremendous research efforts over the last years have clarified many aspects about the mechanism of superconductivity in MgB$_2$ (for a review see Ref. 1). *S*-wave pairing caused by electron-phonon coupling was established soon after the discovery of superconductivity in MgB$_2$. The Fermi surface was calculated and found to consist of four energy bands. Two of them originate from the in-plane orbitals of the boron atoms and are denoted as σ bands. These bands have a cylindrical shape and are strongly anisotropic. On the other hand, the boron p_z orbitals forming the π bands are more isotropic. Today it is experimentally and theoretically established that the anisotropic shape of the Fermi surface together with an anisotropic electron-phonon coupling on the different sheets of this Fermi surface leads to two energy gaps of different size. The gap in the π bands, Δ_π, is about 2 meV, whereas the gap in the σ bands, Δ_σ, is about 7 meV due to the strong coupling to the E_{2g} phonon mode. Considering the nearly equal density of states of these different bands at the Fermi level, this results in the two-band behavior of MgB$_2$. Interband coupling is sufficiently weak to avoid smearing the two-band effects, but is still responsible for a common closing of both energy gaps at the same temperature in zero field.

Soon after the discovery of superconductivity in MgB$_2$ chemical doping was used as a possibility to gain further insight into the unique properties of this material. In the case of carbon substitution, which is described by the structural formula Mg(B$_{1-x}$C$_x$)$_2$, it is established that carbon definitely enters the MgB$_2$ structure.[2] Furthermore two-band superconductivity is retained at least up to a carbon content of 10% (x=0.1), indicating that interband scattering remains small. Higher doping concentrations are discussed controversially.[3–7]

The effects of carbon doping on MgB$_2$ can be summarized as follows: The carbon atoms substitute boron at the boron lattice sites (defining the crystallographic ab plane),

which leads to a linear decrease of the a-axis lattice parameter.[8,9] One main effect on the superconducting properties is enhanced impurity scattering due to lattice distortions in the boron sublattice by chemical disorder. In a two-band superconductor, at least three different scattering rates have to be considered:[10] intraband scattering within π and σ bands and interband scattering between π and σ bands. The retention of two-band superconductivity supports the conclusion that interband scattering is hardly influenced by doping. It is most likely that intraband scattering increases, but it is still under discussion which of the energy bands is affected most. Based on theoretical predictions[11,12] it is argued (cf. for example, Ref. 13) that the π band becomes much dirtier, whereas Ref. 14 provides experimental support for the fact that intraband scattering in the σ band is enhanced by carbon doping. Despite this still open question, several studies have shown an increase in H_{c2} in polycrystalline materials[2,15,16] as well as in single crystals,[8,13,17,18] which could be related to increased intraband scattering. A second important effect of carbon substitution is electron doping by the additional electron provided by the carbon atom. According to predictions of band structure calculations[19] electron doping mainly affects the holes in the σ bands which are continuously filled. This results in a shift of the Fermi level, making the Fermi surface more isotropic. Therefore, a reduced anisotropy[8,9,13,17,18] is found for carbon-doped MgB$_2$ due to a decrease of the σ band anisotropy with increasing carbon substitution.

Two-band superconductivity leads to a number of unusual effects—for example, field-dependent reversible parameters, as was already shown for unsubstituted MgB$_2$ (cf. for example, Refs. 20–23). A simple approach to describe such temperature- and field-dependent parameters is to distinguish between a low-field and a high-field regime. In the low-field regime we assume that the smaller energy gap Δ_π is fully developed and leads, together with Δ_σ, to "low-field" parameters denoted further on by $\sigma\pi$. At high fields, Δ_π is mostly

TABLE I. Sample properties of three differently carbon-doped $Mg(B_{1-x}C_x)_2$ single crystals.

	x	T_c (K)	ΔT_c (K)	m (μg)	$a \times b \times c$ (μm^3)
C1	0.038	35.40	2.4	88	$960 \times 500 \times 67$
C2	0.066	33.15	4.0	58	$680 \times 440 \times 73$
C3	0.095	30.57	7.0	25	$580 \times 260 \times 46$

suppressed (we consider the influence of Δ_π to become vanishingly small), leading to "high-field" parameters which will be denoted by the index σ. We are aware of the fact that such an approach neglects the influence of Δ_π, which decreases continuously with increasing field and thus continuously changes the reversible parameters of such a system. But at least the parameters in the two extreme cases of fields near the lower and upper critical fields can be assessed.

The possibility of suppressing the smaller energy gap Δ_π in external magnetic fields has already been experimentally proved by directional point-contact spectroscopy.[4,24] These experiments also showed a varying influence of the smaller energy gap Δ_π compared to Δ_σ with changing carbon substitution. Heat capacity data[2] also confirm the suppression of Δ_π in external fields.

This paper presents magnetization and torque measurements on three differently carbon-doped MgB_2 single crystals for fields parallel and perpendicular to the ab plane. The magnetic measurements were performed as a function of temperature and external fields; the angular-dependent torque was measured at fixed temperatures and fields. The reversible properties are determined for the two cases of low and high external fields. They are found to follow a "single-band description," if we consider the low- and high-field regimes separately. The dependence of the reversible parameters on the carbon substitution level is investigated.

II. EXPERIMENT

The carbon-doped $Mg(B_{1-x}C_x)_2$ single crystals were grown at the Solid State Laboratory ETH-Zurich using a high-pressure technique in a cubic anvil press. Details can be found in Refs. 8 and 25. The mass, the estimated sample dimensions, the transition temperature T_c, and the width of the superconducting transition ΔT_c are summarized in Table I. The transition temperature was obtained from ac susceptibility measured in a commercial 1-T superconducting quantum interference device (SQUID) magnetometer (Quantum Design) with a special low-field option. The applied ac-field amplitude was 30 μT, and the onset of a tangent criterion was used to evaluate T_c. Here the steepest slope in the transition of the in-phase susceptibility is linearly extrapolated to zero magnetization, where the intersection point of the tangent with the x axis defines T_c. The transition temperature decreases linearly with increasing carbon content; a decrease of 1 K in T_c is found to correspond to the addition of 1.2% carbon. The transition width is defined by the drop of the in-phase susceptibility from 10% to 90% of the Meissner signal. It increases with carbon concentration, indicating that
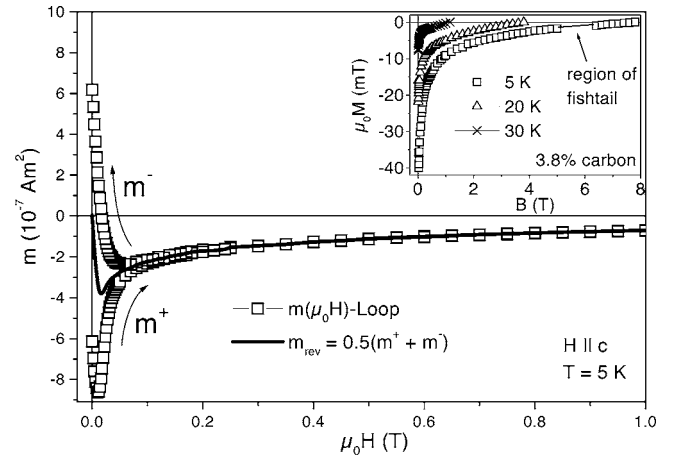

FIG. 1. Evaluation of the reversible magnetic moment from loop measurements. The inset shows the reversible magnetization as a function of the magnetic induction for the entire field range at different temperatures; the region of the fishtail at high fields and low temperatures is indicated by an arrow.

doping at a higher substitution level is probably less homogeneous. For measurements in fields up to 8 T a noncommercial SQUID magnetometer was used; for more experimental details cf. Ref. 26.

Results on undoped MgB_2, which will be compared with the carbon-doped samples, are taken from the single-crystal work reported in Ref. 20.

In general, all experimental data were obtained from magnetization measurements in two SQUID magnetometers; only Fig. 8, below, also shows a comparison with data obtained from torque measurements. These two different techniques were used to assess the reversible parameters in the entire range of the phase diagram, because SQUID magnetometry is limited to fields below 8 T in our system. In addition, an independent confirmation of the evaluation by comparing results from different measurement methods is always useful.

The reversible magnetization, which is needed for evaluations later on, is obtained by measuring the magnetic moment as a function of the applied field at fixed temperatures in a SQUID (loop measurements). The magnetic moments in increasing (m^+) and decreasing fields (m^-) are used to calculate the reversible moment from $m_{rev} = 0.5(m^+ + m^-)$. Carbon-doped MgB_2 shows a smaller irreversible range at low fields than undoped MgB_2; the irreversibility field is about 0.3 T for $H \| c$ at 5 K for sample C2. Therefore, the reversible magnetization is directly accessible over most of the field range. The irreversibility at low fields remains small, thus making the calculation of m_{rev} still very reliable. The hysteretic behavior below the upper critical field (fishtail effect), which is a common feature of carbon-doped MgB_2 (cf. for example, Ref. 8), is excluded from the evaluation. Figure 1 shows an example of the evaluation of the reversible magnetic moment as a function of the applied field up to 1 T and demonstrates the irreversibility at low fields. The reversible magnetization $\mu_0 M$ as a function of the magnetic induction B is derived from $\mu_0 M = \mu_0 m_{rev}/V$. Here V denotes the sample volume and the magnetic induction is given by $B = \mu_0[H + (1$
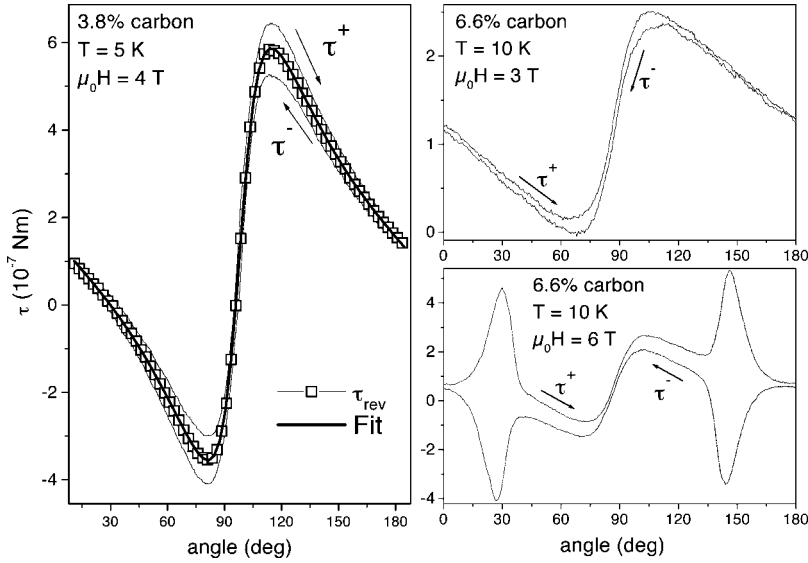
FIG. 2. Torque measurement on sample C1 at 5 K and 4 T (left panel). The reversible torque is calculated from the irreversible branches. The right panels show results on sample C2: a nearly reversible torque at 10 K and 3 T (top) and a torque measurement at 10 K and 6 T, which shows a large hysteretic behavior (bottom).

$-D)M]$ with the demagnetization factor D of the sample. The reversible magnetization versus the magnetic induction B is shown in the inset of Fig. 1, where the reversible curves up to 8 T are compared at three different temperatures for sample C1. The region where the fishtail appears at low temperatures is indicated by an arrow.

To assess the reversible parameters from experimental SQUID data, one-band Ginzburg Landau (GL) and London theories were applied. This is reasonable at high fields, where we assume the smaller energy gap Δ_π to be mostly suppressed and the behavior of the superconducting properties dominated by the larger gap Δ_σ. At low fields near the lower critical field, where both energy gaps definitely have to be taken into account, it is not *a priori* clear whether or not a one-band description could properly describe the superconducting properties. However, fitting the experimental data to a one-band description, we find good agreement by fitting the low- and high-field regions independently (cf. Fig. 5) as already found for undoped MgB$_2$.[20] In addition, according to Ref. 21, the differences between a one- and a two-band description are small enough to justify the employment of a one-band model.

Applying GL theory the reversible magnetization $M(B)$ was calculated from the interpolation formulas given by Brandt:[27]

$$M = (1 - w)M_{low} + wM_{high}, \tag{1}$$

$$w = 0.5 + 0.5 \, \text{erf}[2(2b\kappa^2 - 1)], \tag{2}$$

$$b = \frac{B}{B_{c2}}, \tag{3}$$

$$M_{low} = -H_{c1} + b - \frac{3\sqrt{\pi c}}{2\kappa^2}e^{-c}\left(1 + \frac{19}{8c} - \frac{47}{128c^2}\right), \tag{4}$$

$$c = \sqrt{\frac{4\pi}{\sqrt{3}b\kappa^2}}, \tag{5}$$

$$H_{c1} = \frac{\Phi_0}{4\pi\mu_0\lambda^2}(\ln\kappa + \alpha), \tag{6}$$

$$\alpha = 0.49693 + \exp[-0.41477 - 0.775\ln\kappa - 0.1302(\ln\kappa)^2], \tag{7}$$

$$M_{high} = -\frac{H_{c2}}{4\kappa^2}\ln\left(1 + \frac{1-b}{b}(0.357 + 2.89b - 1.581b^2)\right). \tag{8}$$

Fitting this reversible magnetization to the experimental data, B_{c2} and κ are obtained as fit parameters and from these values all other parameters can be calculated.

The London relations used for the evaluation of the penetration depth in the high-field regime are given by

$$\frac{\partial M^c}{\partial\ln(B)} = \frac{\phi_0}{8\pi\mu_0\lambda_{ab}^2}, \tag{9}$$

$$\frac{\partial M^{ab}}{\partial\ln(B)} = \frac{\phi_0}{8\pi\mu_0\lambda_{ab}\lambda_c}, \tag{10}$$

where M^c and M^{ab} denote the magnetization in fields parallel and perpendicular to the c axis, respectively.

The torque measurements were performed in a 9-T PPMS System (Quantum Design) at the Institute of Physics of the Polish Academy of Sciences. The angular-dependent torque was measured at fixed external fields and temperatures; Fig. 2 presents three examples of such results. The torque is recorded while rotating the *ab* plane of the sample from $-90°$ to $+90°$ with respect to the external field direction (τ^+) and again back to the initial position (τ^-). Ten measurements are averaged at one position; the interval between two points is $0.5°$. The reversible torque is calculated from the irreversible branches from $\tau_{rev} = 0.5(\tau^+ + \tau^-)$ (squares in the left panel of Fig. 2; only 20% of the points are shown for clarity and the symbol size represents the standard deviation).

Fitting reversible torque curves to anisotropic London theory (bold line in the left panel of Fig. 2), the penetration depth anisotropy $\gamma_\lambda = \lambda_c / \lambda_{ab}$, $\mu_0 H_{c2}^c$ and the in-plane penetration depth λ_{ab} can be obtained as fit parameters.[28] The equations for fitting the torque are

$$\tau_{rev}(\varphi) = -\frac{H\phi_0}{16\pi\lambda_{ab}^2}(1-\gamma^{-2})\frac{\sin 2\varphi}{\epsilon_\varphi}\ln\left(\frac{\eta H_{c2}^c}{\epsilon_\varphi H}\right), \quad (11)$$

$$\epsilon_\varphi = \sqrt{\gamma^{-2}\sin^2(\varphi) + \cos^2(\varphi)}. \quad (12)$$

The parameter η depends on the flux-line lattice symmetry and is approximately 1. This evaluation is only valid for reversible torque curves, and some error might be introduced by calculating the reversible torque from the irreversible branches. To obtain more reliable results the background was measured and subtracted. Furthermore, the upper critical fields were taken from SQUID measurements and used as input parameters in the fitting procedure. Problems that may arise from such an evaluation for carbon-doped samples will be discussed in Sec. III C, but as can be seen in Fig. 2, we find good agreement between the fit and the experimental data.

III. REVERSIBLE MIXED-STATE PROPERTIES

A. Upper critical field and coherence length

SQUID measurements of the magnetic moment as a function of temperature at fixed applied field were taken to determine the upper critical field $H_{c2}(T)$. The onset of the superconducting signal in the $m(T)$ curve at a certain magnetic field is used to define the critical temperature $T_c(\mu_0 H_a)$. A second method for evaluating $T_c(\mu_0 H_a)$ consists of extrapolating the linear decrease of the magnetization below the superconducting transition to the x axis with zero magnetization. The latter leads to temperature data that are smaller by 0.5–1 K (depending on the applied field and the field direction) than the results obtained from the onset criterion. The difference between these two methods is smaller than the size of the symbols used in Fig. 3, which presents the results of the onset criterion. The $H_{c2}(T)$ curves are shown for fields parallel (solid symbols) and perpendicular (open symbols) to the ab plane of the single crystals. For better comparison the reduced temperature T/T_c was chosen as the x axis and the upper critical field of an undoped MgB_2 single crystal is also shown.

For fields $H \| c$, H_{c2}^c increases with increasing carbon concentration. On the other hand, for fields within the ab plane H_{c2}^{ab} increases only at low doping levels, but decreases again above 3.8% carbon substitution. Results on polycrystalline material,[16] where the carbon content was changed between 0.5% and 3.8%, showed a monotonous increase in H_{c2}, which corresponds to H_{c2}^{ab}. Measurements on single crystals[29] with carbon concentrations between 2% and 7.5% showed a maximum of H_{irr}^{ab} between 2% and 5% carbon (H_{irr}^{ab} denotes the irreversibility field close to H_{c2}). Hence, the available data indicate that the maximum in H_{c2}^{ab} occurs at around 4% carbon. The inset of Fig. 3 shows the dependence of $\delta H_{c2}(0)$,
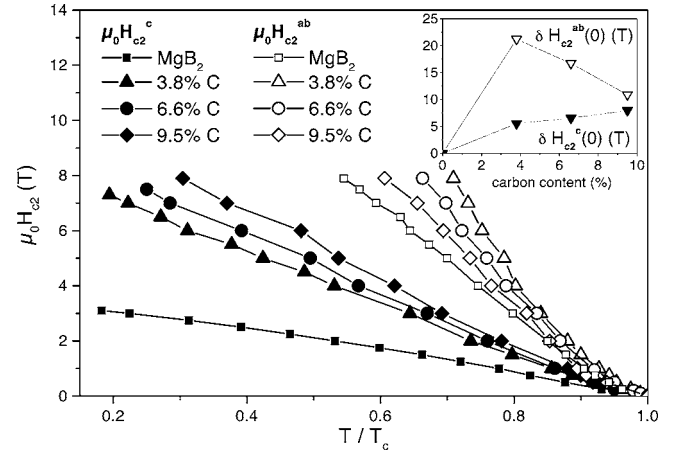

FIG. 3. Upper critical field as a function of the reduced temperature T/T_c. The solid symbols refer to $H \| c$, open symbols to $H \| ab$. For comparison the upper critical field of an undoped MgB_2 single crystal is shown as well (squares). The inset shows $\delta H_{c2}(0)$ as a function of carbon content for both field orientations.

defined as the increase of the upper critical field compared to undoped MgB_2 at zero temperature, on the carbon content for both field orientations. A nearly linear increase of $H_{c2}^c(0)$ ($\sim +0.43$ T per 1% carbon for a carbon content above 3.8%) and also a quite linear decrease of $H_{c2}^{ab}(0)$ (~ -1.8 T per 1% carbon for $\geq 3.8\%$ carbon) are found in the investigated range of carbon substitutions. The experimental data points were fitted to the function $H_{c2}(t) = H_{c2}(0)(1-t^\alpha)^\beta$ to obtain $H_{c2}(0)$ [$t = T/T_c$; α, β, and $H_{c2}(0)$ are fit parameters]. For $H \| ab$ the upturn of H_{c2}^{ab} near T_c was not included in the fitting procedure and therefore T_c was allowed to vary freely.

The high-field coherence length can be determined from the upper critical field within GL theory in a straightforward way from $\mu_0 H_{c2}^c = \phi_0/2\pi\xi_{ab}^2$ and $\mu_0 H_{c2}^{ab} = \phi_0/2\pi\xi_{ab}\xi_c$. Figure 4 shows the results for fields parallel and perpendicular to the crystallographic c axis. The in-plane coherence length ξ_{ab} significantly decreases from undoped MgB_2 to 3.8% carbon substitution by nearly 50%. At higher substitution levels the further decrease of ξ_{ab} is smaller and nearly linear with car-
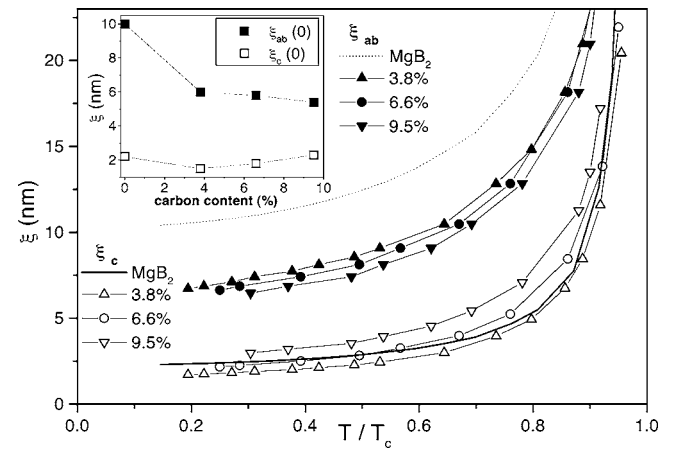

FIG. 4. Coherence lengths determined from the upper critical fields. The inset shows the dependence of $\xi(0)$ on carbon content.

bon concentration ($\sim$10% in the investigated doping range from 3.8% to 9.5%). The coherence length in the c direction, ξ_c, reflects the dependence of the upper critical field on carbon doping. For low doping levels, ξ_c decreases compared to MgB$_2$, but at higher carbon contents it increases again monotonously. These results are plotted in the inset of Fig. 4 for zero temperature.

To interpret the dependence of the upper critical fields on the carbon content, two mechanisms can be considered. First, the relationship between the coherence length ξ and the mean free path l for electron scattering, $\xi \propto \sqrt{\xi_0 l}$, where ξ_0 denotes the coherence length in the clean limit, shows that the upper critical field increases when reducing the coherence length due to an increased intraband scattering rate and a reduced mean free path. On the other hand, ξ_0 is related to the energy gap by $\xi_0 \propto v_F/\Delta$ (v_F denotes the Fermi velocity). Thus a reduced condensation energy by decreased energy gaps at higher doping levels[3,4] can overcome this effect of the impurities. Then H_{c2} decreases again by an enlarged coherence length ξ_0. Apparently this scenario, which neglects possible changes in v_F, can describe the data on polycrystalline material and single crystals for $H \| ab$, leading to the observed maximum in H_{c2} (l decreases with doping, ξ_0 increases with increasing carbon content by the decreased energy gaps). For $H \| c$, the single crystals show monotonously increasing upper critical fields, which could indicate a much larger decrease of the mean free path within the ab plane compared to the c direction. For this field orientation the decrease of the condensation energy seems to be less important compared to the effect from the introduction of defects.

An alternative explanation is related to electron doping. The shifted Fermi surface and, hence, the changed Fermi velocity v_F (more precisely $v_F^{\|ab}$ for $H \| c$) are related to H_{c2} by $H_{c2} \propto v_F^{-2}$. Thus changes in the upper critical field can be related to electron doping as well.

We cannot draw definite conclusions from our results on which of the two scenarios is responsible for the dependence of H_{c2} on the carbon content. Results on Al-doped MgB$_2$ show a similar dependence of T_c and the anisotropy on the additional electron content provided by the substituted elements (see, e.g., Ref. 13). Therefore, electron doping can account for these effects. But the completely different behavior of H_{c2} in Al- and C-doped samples also shows that the effect of impurities cannot be neglected in carbon-doped MgB$_2$. Most probably electron doping is mainly responsible for the changes in T_c and the anisotropy in carbon-doped samples, because these quantities behave similarly in Al- and C-doped MgB$_2$, whereas the observed behavior of H_{c2} can only be understood by taking into account the influence of impurities on the electron mean free path due to increased intraband scattering.

B. Penetration depth

The penetration depth is evaluated in two different ways for the low-field and high-field regimes, respectively. For low fields, we apply one-band GL theory modeled by the interpolation formulas by Brandt [cf. Eqs. (1)–(8) in Sec. II]. Figure 5 shows the reversible magnetization and the best GL
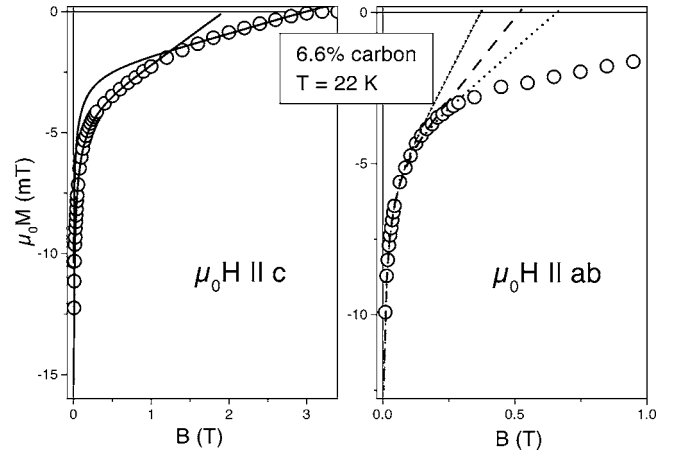

FIG. 5. Reversible magnetization at 22 K for sample C2 in fields applied parallel (left panel) and perpendicular (right panel) to the c axis. The best GL fits for the low-field and high-field regimes are shown for $H \| c$. For $H \| ab$ the influence of the fit interval on the GL fits is indicated by the dotted lines.

fits to the low- and high-field regimes at 22 K for $H \| c$ for sample C2 as an example for such an evaluation on carbon-doped crystals. For $H \| ab$ only the fit to the low-field regime is displayed and the influence of the field range used for the fit is indicated by the dotted lines.

The penetration depths $\lambda_{ab}^{\sigma\pi}$ and $\lambda_c^{\sigma\pi}$ are calculated from the GL relations $\kappa^c = \lambda_{ab}/\xi_{ab}$ and $\kappa^{ab} = \sqrt{\lambda_{ab}\lambda_c/\xi_{ab}\xi_c}$. The upper boundaries of the fit interval for the low-field regime are found to be $H_{c2}^c/10$ and $H_{c2}^{ab}/100$ for the corresponding field directions. This results in the best GL fits. Therefore, these limits were employed throughout the entire evaluation, in order to get comparable results for the differently doped crystals.

Such an analysis is in principle also possible for the high-field regime, but was not employed for two reasons. First, magnetic fields needed to measure loops up to H_{c2}, especially for $H \| ab$, are not accessible. Second, the reversible magnetization at high fields becomes rather small and approaches the resolution limit of our SQUID. Therefore, κ and H_{c2} were evaluated only in some cases for the high-field regime by fitting magnetization loops to GL theory (these values correspond to the results of Sec. III D within estimated error bars).

For determining the penetration depth in the high-field regime we adopt a different approach using London theory. The reversible magnetization was now measured as a function of temperature at various applied fields up to 8 T. From these results, the magnetization as a function of the applied field can be extracted at fixed temperature. The experimentally observed linear variation of the reversible magnetization M with $\ln(B)$ in the field range considered justifies the application of London theory for the evaluation of the penetration depths in the high-field regime, λ_{ab}^σ and λ_c^σ, from Eqs. (9) and (10) in Sec. II. The penetration depth anisotropy $\gamma_\lambda^\sigma = \lambda_c^\sigma/\lambda_{ab}^\sigma$ being identical to the upper critical field anisotropy γ_H for the high-field regime (see the following paragraph) indicates that $M(T)$ measurements in fields up to 8 T indeed lead to the penetration depth of the high-field regime.
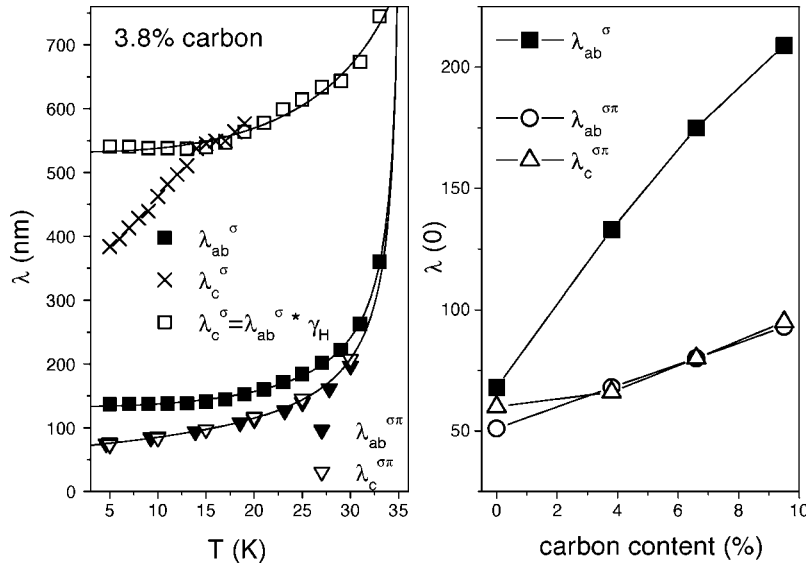
FIG. 6. Penetration depth for sample C1 (left panel). The triangles refer to the low-field regime and the squares denote high-field values; λ_c^σ is calculated from λ_{ab}^σ and anisotropy (see text). The right panel shows the dependence of $\lambda(0)$ on carbon content.

The left panel in Fig. 6 shows the penetration depth of sample C1. The triangles display results from fitting the low-field reversible magnetization to the GL expression; the squares refer to the London evaluation for the high-field regime. In both cases the solid symbols indicate the penetration depth λ_{ab} within the crystallographic *ab* plane and the open symbols the penetration depth λ_c.

The evaluation of λ_c^σ needs some further comments. In principle a fixed field range—e.g., from $H_{c2}/3$ to H_{c2}—should be applied for evaluating the penetration depth at different temperatures. This is again difficult, especially for $H \| ab$, because of the high upper critical fields and the small reversible magnetization at higher temperatures, which leads to large errors. Therefore, the evaluation was restricted to low temperatures. The crosses in Fig. 6 indicate data directly evaluated from $M(T)$ measurements obtained between 5 and 20 K and in the field range from 3 to 8 T. We find a strong temperature dependence for λ_c^σ at lower temperatures. On the contrary, when calculating λ_c^σ from λ_{ab}^σ and anisotropy γ_H (cf. Fig. 7), we find the data indicated by the open squares. These values are comparable to the directly evaluated ones, but only at temperatures between 13 and 20 K. We assume that at temperatures below 13 K the applied fields are not large enough to obtain the correct λ_c^σ from $M(T)$ measurements. This leads to the strong decrease of λ_c^σ at low tempeartures and reflects the field dependence of the penetration depth (furthermore, errors from applying London theory cannot be excluded as well). In view of these findings, λ_c^σ is calculated in the following from λ_{ab}^σ and anisotropy.

The results of such evaluations for samples C2 and C3 are shown in the right panel of Fig. 6. Generally, the penetration depth increases with increasing carbon content in the whole field and temperature range as well as for both field directions. This is expected and can be understood by electron doping using the London relation $\lambda = \sqrt{m_e / \mu_0 e^2 n_s}$, where n_s denotes the superconducting charge carrier density. The loss of holes due to band filling with increasing carbon concentration should be related to a loss of superconducting charge carriers. Thus λ is continuously enhanced as observed. Trying to reproduce λ_{ab}^σ by a reduction of n_s due to the addi-

tional electrons provided by carbon substitution leads to the right tendency for the penetration depth, but is not sufficient to match the experimental data. This is not really expected, since changes in the Fermi surface will also lead to changes in the effective electron mass m_e, which are difficult to take into account.

The penetration depth in the low-field regime $\lambda^{\sigma\pi}(0)$ increases almost linearly with carbon content. It becomes isotropic at the lowest doping level of 3.8% carbon, which is also displayed in the left panel of Fig. 6. The low-field penetration depth is identical within experimental error for both field directions. According to the above London relation between the penetration depth and the superconducting charge carrier density, the smaller low-field penetration depth (compared to that in the high-field regime) indicates that the density of the superconducting charge carriers is significantly reduced with increasing field due to the missing carriers from the π gap.
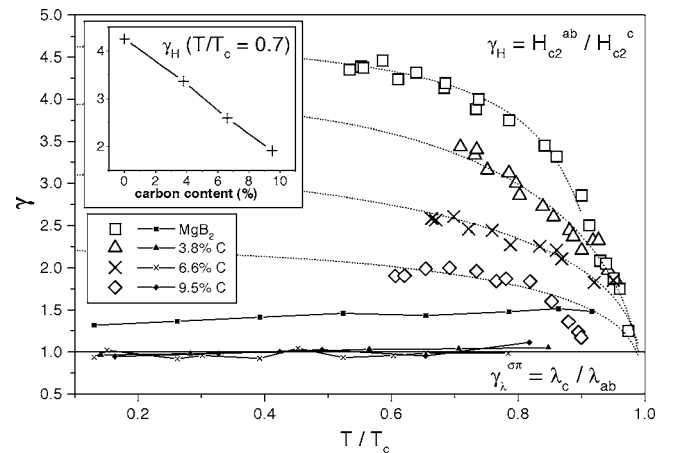

FIG. 7. Anisotropy of undoped and carbon-doped MgB$_2$. The large symbols refer to results evaluated from the upper critical fields (γ_H); the dotted lines indicate the anisotropy down to low temperatures evaluated from extrapolated H_{c2}^{ab} values. The small symbols refer to the penetration depth anisotropy $\gamma_\lambda^{\sigma\pi}$ at low fields (see text). The inset shows the anisotropy γ_H as a function of carbon substitution at $T/T_c = 0.7$.

The results for the penetration depth in the high-field regime, λ_{ab}^{σ}, are supported by the torque measurements (cf. Sec. II). The values for λ_{ab}^{σ} at 5 K differ from the above data by about 3% for sample C1 and by 12% for sample C3, which represents the worst case, because it refers to the smallest sample and hence to the smallest signal-to-background ratio in the torque experiment. In addition to the torque results, further confirmation for λ_{ab}^{σ} comes from the fact that the above data lead to $\gamma_{\lambda}^{\sigma} = \gamma_H$ (at least in a small temperature range—see next paragraph).

C. Anisotropy

The anisotropy $\gamma_H = H_{c2}^{ab}/H_{c2}^{c}$ was evaluated from the upper critical fields. Figure 7 shows the results for undoped MgB$_2$ and carbon-doped samples (large symbols). The dotted lines indicate the calculated anisotropy from fitting and extrapolating H_{c2}^{ab} to zero temperature. The anisotropy decreases continuously with increasing carbon content, which is attributed to the decrease of the Fermi surface anisotropy, especially in the σ band. The inset of Fig. 7 shows the decrease of γ_H as a function of carbon content at $T/T_c = 0.7$, which refers to the directly accessible region of the phase diagram with our equipment, but these values also do not change a lot to lower temperatures.

The results for γ_H at low temperatures and the identity $\gamma_H = \gamma_{\lambda}^{\sigma}$ are supported by torque measurements. The anisotropy obtained by fitting reversible torque curves to anisotropic London theory (see Sec. II) is in excellent agreement with the results from SQUID measurements on undoped MgB$_2$ (cf. Ref. 30) and confirm that $\gamma_H = \gamma_{\lambda}^{\sigma}$ at all temperatures. The situation is more difficult for carbon-doped single crystals. First of all, the magnetization becomes irreversible at fields below the upper critical field (fishtail effect), thus limiting the field range where this fitting procedure is valid. Second, as already discussed in Sec. I, there is some evidence that the smaller energy gap Δ_{π} influences the sample properties up to higher fields in carbon-doped samples than in undoped MgB$_2$. This results in data for γ_{λ} that are highly dependent upon the external field over a large field range (in undoped MgB$_2$ this was only observed for fields below 1 T at 5 K). Thus, these experiments directly trace the field dependence of the anisotropy, but they can only be used in a rather limited field and temperature range to support the results from SQUID measurements (e.g., for sample C1 at $\leqslant$5 K and around 4 T). At temperatures above 5 K, we could not find any field region where the anisotropy determined from torque did not depend on the external field (at lower fields the changing influence of the π gap affects the anisotropy, whereas at higher fields the torque becomes irreversible due to the fishtail effect), leading to anisotropy data that were always lower than those from SQUID measurements. So in torque only at low temperatures ($\sim$5 K) a small field region was found, which is not affected by the changing influence of Δ_{π} and still reversible, leading to similar values of anisotropy in this small field interval. At least in this case the extrapolated anisotropies determined from SQUID measurements could be confirmed and the extrapolation of the upper critical fields for $H\|ab$ justified. The anisotropy for
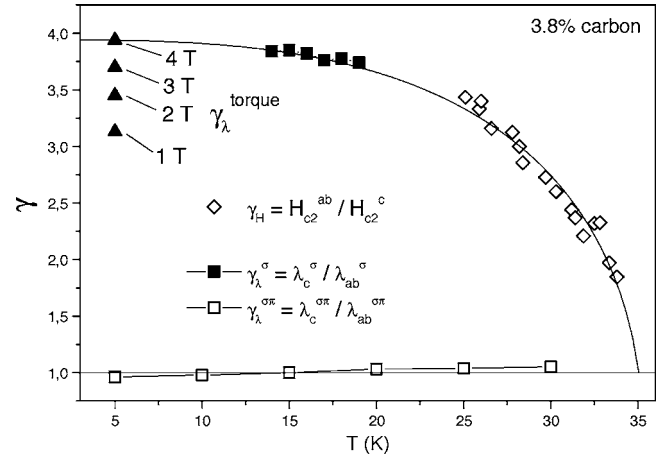

FIG. 8. Anisotropy of sample C1 obtained from different evaluation methods. The squares refer to the penetration depth anisotropy γ_{λ} for the low-field (open squares) and high-field regimes [solid squares, directly evaluated from $m(T)$ measurements]. The anisotropy γ_H (obtained from the upper critical fields) is denoted by diamonds, and the triangles indicate results from torque measurements at 5 K and at various applied fields between 1 and 4 T.

sample C1 determined by torque at 5 K and various fields is plotted in Fig. 8 and compared with data from magnetization measurements.

Furthermore, the anisotropy derived from the upper critical fields and from the torque experiment is compared with the penetration depth anisotropy $\gamma_{\lambda} = \lambda_c/\lambda_{ab}$. For the high-field regime $\gamma_{\lambda}^{\sigma}$ could be determined only in a small temperature range (cf. the solid squares in Fig. 8) for reasons already discussed before. We find that $\gamma_{\lambda}^{\sigma}$ agrees quite well with γ_H. The penetration depth anisotropy in the low-field regime, $\gamma_{\lambda}^{\sigma\pi}$, is nearly isotropic for all three carbon-doped samples over most of the temperature range. This is attributed to the increased influence of the more isotropic π band. There is some indication that $\gamma_{\lambda}^{\sigma\pi}$ approaches γ_H close to T_c and that the low-field anisotropy exhibits the opposite temperature dependence to the high-field regime. This was theoretically predicted in Ref. 31. The results indicate that $\gamma_{\lambda}^{\sigma\pi}$ slightly increases and meets the values of γ_H at T_c, but there are not enough data points to confirm this definitely. In fact, the estimated error bars for $\gamma_{\lambda}^{\sigma\pi}$ are quite high (± 0.3). The low-field anisotropy calculated from the hypothetical upper critical fields, obtained by fitting the low-field part of the reversible magnetization to GL theory, is in agreement with $\gamma_{\lambda}^{\sigma\pi}$ within this error interval.

The assumption of one-band London and GL theory—i.e., that the penetration depth anisotropy γ_{λ} and the upper critical field anisotropy γ_H are the same—is not necessarily true in general. Taking all our data into account, we deduce that $\gamma_H = \gamma_{\lambda}$, but both are field dependent; i.e., a certain value depends strongly upon the measurement method and the parameters relevant for this measurement. The anisotropy in low applied fields is small and close to 1, whereas at high fields anisotropy is significant. At the transition temperature, the data for the low-field and high-field regimes seem to merge at a common value.
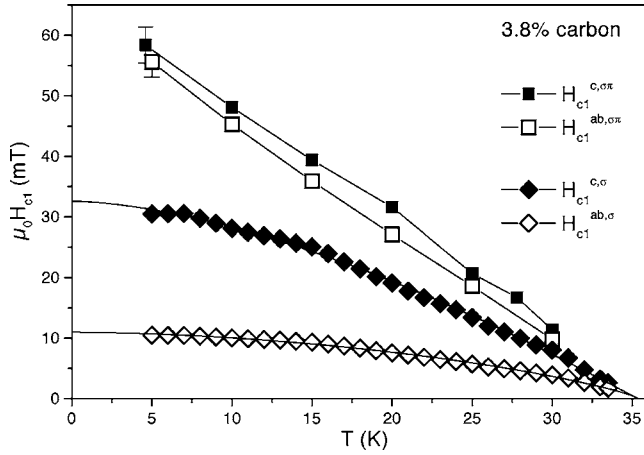
FIG. 9. Lower critical fields for sample C1. Solid symbols refer to $H\|c$, open symbols to $H\|ab$.

D. Lower critical field H_{c1}, thermodynamic critical field H_c, and GL parameter κ

The lower critical field H_{c1} in the two field regimes was calculated from $\mu_0 H_{c1}^c = (\Phi_0/4\pi\lambda_{ab}^2)(\ln\kappa^c + \eta)$ and $\mu_0 H_{c1}^{ab} = (\Phi_0/4\pi\lambda_{ab}\lambda_c)(\ln\kappa^{ab} + \eta)$ with η set to 0.5.[27] Note that only the lower critical field for the low-field regime refers to the field where the first flux lines are formed within a superconductor (denoted as the penetration field which is related to the field commonly interpreted as H_{c1}). The lower critical field for the high-field regime is more difficult to interpret because no transition from the Meissner state to the mixed state occurs in the high-field regime. Possibly these data indicate a tendency as to which values the lower critical fields would achieve if the smaller energy gap were absent.

The results for sample C1 are plotted in Fig. 9. For the high-field regime we find a parabolic dependence on temperature and that the system becomes more isotropic with increasing carbon content. For the low-field regime, H_{c1} is larger than in the high-field regime and shows a rather linear dependence on temperature. The error bars at low temperatures indicate the dependence of the evaluation on the fit interval. Within these error bars the results for $H\|c$ and $H\|ab$ are identical, suggesting that the lower critical field is isotropic in the low-field regime already at a carbon concentration of 3.8%. The lower critical fields for samples C2 and C3 show a similar dependence on temperature, but the curves are shifted to lower fields with increasing carbon content, leading to a decrease of H_{c1} at higher doping levels in the entire temperature and field range. The left-hand panel in Fig. 10 shows the dependence of $H_{c1}(0)$ on increasing carbon substitution.

The thermodynamic critical field H_c was calculated by integrating the area under the reversible magnetization curve. The right-hand panel in Fig. 10 shows the results for undoped MgB_2, samples C1 and C2. The condensation energy decreases with increasing carbon content. The results show quite large errors, especially at low temperatures, where the upper critical fields are high and the reversible magnetization small. Differing results at nearby temperatures can be assumed to represent the error bars. Estimating the decrease of the critical field from the decrease of the transition temperature ($\mu_0 H_c \propto T_c$, if changes in the density of states at the Fermi level are neglected) leads to a similar result for $H_c(0)$ in sample C1, but to a higher value for sample C2 compared to the result presented in the right-hand panel of Fig. 10. Due to the sensitivity of this evaluation to the exact sample volume, it could be possible that small errors in the mass of sample C2 (which has the smallest mass of the three samples which are compared) lead to too low values for the critical field and that the decrease of the condensation energy is more linear than expressed in Fig. 10.

Figure 11 exemplarily presents the GL parameter κ for sample C1 as a function of temperature; the inset shows the dependence of $\kappa(0)$ on carbon substitution. The GL parameter generally increases with increasing carbon substitution in the whole temperature and field range and for both field directions. The error bars for the low-field data again indicate the influence of the fit interval. The results also suggest that κ tends towards a common value $\kappa(T_c)$ for both field orientations and for the entire field range. This value is given in Table II in the following section.
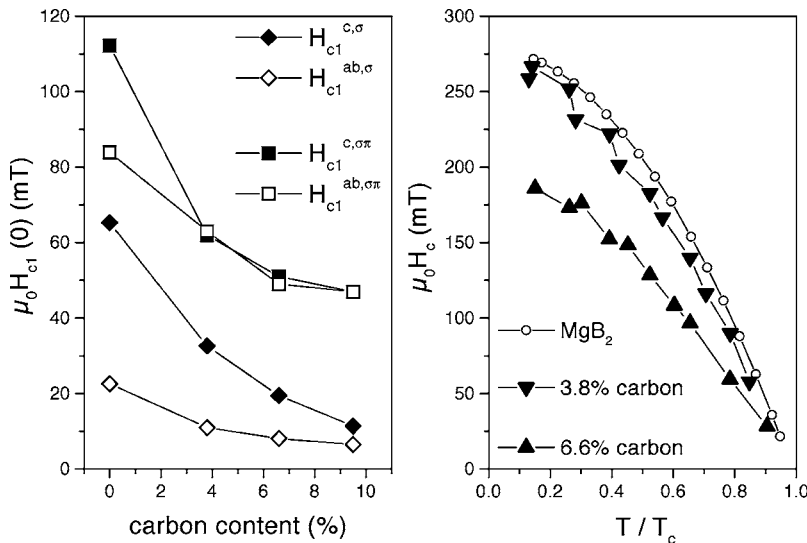

FIG. 10. Lower critical fields at $T=0$ K as a function of carbon substitution (left panel). The right-hand panel shows the decrease of the thermodynamic critical field with increasing carbon content in comparison with undoped MgB_2.
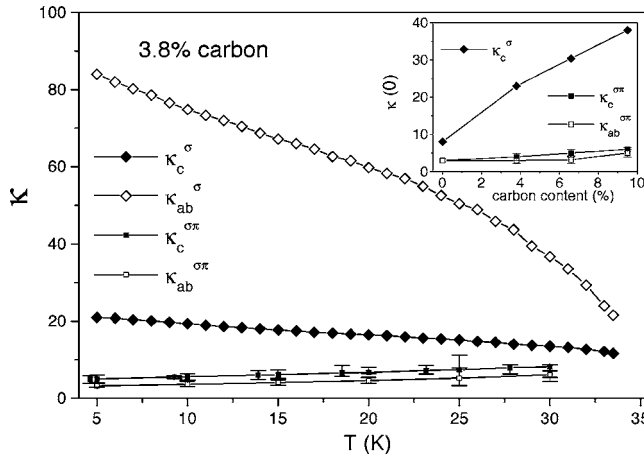
FIG. 11. GL parameter κ for sample C1. The open symbols refer to $H\|ab$, the solid symbols to $H\|c$. The inset shows $\kappa(0)$ as a function of carbon content.

IV. SUMMARY AND CONCLUSION

The anisotropic reversible parameters of three differently carbon-doped $Mg(B_{1-x}C_x)_2$ single crystals were characterized by magnetic and torque measurements. These parameters are found to be essentially field dependent, as in pure MgB_2, due to the persistence of two-band superconductivity in the investigated range of carbon substitution. The reversible parameters were analyzed within a one-band picture in two different field regimes, neglecting the fact that they are continuously changing due to their field dependence in such a two-band superconductor. Furthermore, this simplification allows us to assess the range of these reversible parameters—i.e., to establish data at small fields near the lower critical field and also at large fields near the upper critical field. The low-field values were obtained by fitting the low-field part of the reversible magnetization curves to one-band GL theory. For determining some of the high-field parameters, also London theory was applied. Table II summarizes the reversible parameters in these two field regimes for $Mg(B_{1-x}C_x)_2$ single crystals with $x=0.038$, 0.066, and 0.095. Data for the upper critical fields and the coherence lengths provided in the table refer to the high-field regime. The results for the low-field region are omitted, since their physical meaning is still unclear and an interpretation difficult. Similarly, γ_H refers to the anisotropy in the high-field regime.

The upper critical field for $H\|c$ is enhanced by increasing the carbon concentration. A linear increase for $H_{c2}^c(0)$ of $\sim+0.43$ T by per 1% carbon is found in the investigated range of carbon substitution. For $H\|ab$, the upper critical field H_{c2}^{ab} also increases, but exhibits a maximum at around 3.8% carbon substitution. A linear decrease of $H_{c2}^{ab}(0)$ by

TABLE II. Reversible mixed-state parameters of carbon-doped $Mg(B_{1-x}C_x)_2$ single crystals for applied fields parallel and perpendicular to the ab plane. The low-field values are denoted by $\sigma\pi$, the high-field values by σ.

Carbon	C1 3.8%	C2 6.6%	C3 9.5%	MgB_2
$H_{c2}^c(0)$ (T)	8.9 ± 0.3	9.9 ± 0.3	11.3 ± 0.4	3.3 ± 0.3
$H_{c2}^{ab}(0)$ (T)	35.4 ± 1.4	30.8 ± 1.5	25.0 ± 1.3	14.1 ± 0.8
$\gamma_H(T/T_c=0.7)$	3.4 ± 0.15	2.6 ± 0.1	1.9 ± 0.2	4.3 ± 0.1
$\xi_{ab}(0)$ (nm)	6.0 ± 0.1	5.8 ± 0.1	5.4 ± 0.15	10.7 ± 0.6
$\xi_c(0)$ (nm)	1.5 ± 0.1	1.8 ± 0.2	2.3 ± 0.1	2.3 ± 0.1
$\lambda_{ab}^{\sigma\pi}(0)$ (nm)	68 ± 6	80 ± 6	93 ± 7	51 ± 1
$\lambda_c^{\sigma\pi}(0)$ (nm)	66 ± 19	80 ± 20	95 ± 17	60 ± 4
$\lambda_{ab}^{\sigma}(0)$ (nm)	133 ± 10	175 ± 14	209 ± 15	76 ± 8
$\kappa(T_c)$	9 ± 3	18 ± 5	22 ± 6	≈4.5
$\mu_0H_c(0)$ (mT)	263 ± 14	195 ± 11		300 ± 25
$\mu_0H_{c1}^{c,\sigma\pi}(0)$ (mT)	62 ± 3	51 ± 2	47 ± 2	113 ± 3
$\mu_0H_{c1}^{ab,\sigma\pi}(0)$ (mT)	63 ± 2	49 ± 1	47 ± 1	87 ± 10

~-1.8 T per 1% carbon for $\geq3.8\%$ carbon is found. Two possible mechanisms were discussed, which could lead to this increase in the upper critical fields. The penetration depth increases monotonously with increasing carbon substitution for arbitrary field directions as well as in the whole temperature and field range. This is expected and explained by electron doping and band filling which leads to a continuous decrease of the superconducting charge carriers with increasing carbon content. In general, the anisotropy decreases for the entire field and temperature range with increasing carbon substitution. The penetration depth anisotropy in the high-field regime determined from SQUID measurements corresponds to the upper critical field anisotropy. Further, the anisotropy evaluated from the torque method confirms the high-field anisotropy at low temperatures. Furthermore, the carbon-doped samples are isotropic in the low-field regime over most of the temperature range, but reach the high-field anisotropy just below the transition temperature. Therefore, the anisotropy in this field regime has the opposite temperature dependence from that in the high-field regime. The thermodynamic critical field and the condensation energy decrease with increasing carbon substitution, as does the lower critical field, whereas the GL parameters increase.

*Electronic address: krutzler@ati.ac.at

[1] Physica C **385** (1 and 2) (2003).

[2] R. A. Ribeiro, S. L. Budko, C. Petrovic, and P. C. Canfield, Physica C **384**, 227 (2003).

[3] J. Kortus, O. V. Dolgov, R. K. Kremer, and A. A. Golubov, Phys. Rev. Lett. **94**, 027002 (2005).

[4] R. S. Gonnelli, D. Daghero, A. Calzolari, G. A. Ummarino, V. Dellarocca, V. A. Stepanov, S. M. Kazakov, N. Zhigadlo, and J. Karpinski, Phys. Rev. B **71**, 060503(R) (2005).

[5] Z. Holanova, P. Szabo, P. Samuely, R. H. T. Wilke, S. L. Budko, and P. C. Canfield, Phys. Rev. B **70**, 064520(R) (2004).

[6] G. A. Ummarino, D. Daghero, R. S. Gonnelli, and A. H. Moudden, Phys. Rev. B **71**, 134511 (2005).

[7] H. Schmidt, K. E. Gray, D. G. Hinks, J. F. Zasadzinski, M. Avdeev, J. D. Jorgensen, and J. C. Burley, Phys. Rev. B **68**, 060508(R) (2003).

[8] S. M. Kazakov, R. Puzniak, K. Rogacki, A. V. Mironov, N. D. Zhigadlo, J. Jun, C. Soltmann, B. Batlogg, and J. Karpinski, Phys. Rev. B **71**, 024533 (2005).

[9] S. Lee, T. Masui, A. Yamamoto, H. Uchiyama, and S. Tajima, Physica C **397**, 7 (2003).

[10] I. I. Mazin, O. K. Andersen, O. Jepsen, O. V. Dolgov, J. Kortus, A. A. Golubov, A. B. Kuzmenko, and D. van der Marel, Phys. Rev. Lett. **89**, 107002 (2002).

[11] A. A. Golubov and A. E. Koshelev, Phys. Rev. B **68**, 104503 (2003).

[12] A. Gurevich, Phys. Rev. B **67**, 184515 (2003).

[13] M. Angst, S. L. Budko, R. H. T. Wilke, and P. C. Canfield, Phys. Rev. B **71**, 144512 (2005).

[14] A. V. Sologubenko, N. D. Zhigadlo, S. M. Kazakov, J. Karpinski, and H. R. Ott, Phys. Rev. B **71**, 020501(R) (2005).

[15] Z. Holnova, J. Kacmarcik, P. Szabo, P. Samuely, I. Sheikin, R. A. Ribeiro, S. L. Budko, and P. C. Canfield, Physica C **404**, 195 (2004).

[16] R. H. T. Wilke, S. L. Budko, P. C. Canfield, D. K. Finnemore, R. J. Suplinskas, and S. T. Hannahs, Phys. Rev. Lett. **92**, 217003 (2004).

[17] T. Masui, S. Lee, A. Yamamoto, H. Uchiyama, and S. Tajima, Physica C **412**, 303 (2004).

[18] T. Masui, S. Lee, and S. Tajima, Phys. Rev. B **70**, 024504 (2004).

[19] N. I. Medvedeva, A. L. Ivanovskii, J. E. Medvedeva, and A. J. Freeman, Phys. Rev. B **64**, 020502(R) (2001).

[20] M. Zehetmayer, M. Eisterer, J. Jun, S. M. Kazakov, J. Karpinski, and H. W. Weber, Phys. Rev. B **70**, 214516 (2004).

[21] M. Eisterer, M. Zehetmayer, H. W. Weber, and J. Karpinski, Phys. Rev. B **72**, 134525 (2005).

[22] M. Angst *et al.*, Phys. Rev. B **70**, 224513(R) (2004).

[23] J. D. Fletcher, A. Carrington, O. J. Taylor, S. M. Kazakov, and J. Karpinski, Phys. Rev. Lett. **95**, 097005 (2005).

[24] R. S. Gonnelli, D. Daghero, G. A. Ummarino, V. A. Stepanov, J. Jun, S. M. Kazakov, and J. Karpinski, Phys. Rev. Lett. **89**, 247004 (2002).

[25] J. Karpinski, S. M. Kazakov, J. Jun, M. Angst, R. Puzniak, A. Wisniewski, and P. Bordet, Physica C **385**, 42 (2003).

[26] M. Zehetmayer, F. M. Sauerzopf, J. Karpinski, M. Murakami, and H. W. Weber, Physica C **383**, 232 (2002).

[27] E. H. Brandt, Phys. Rev. B **68**, 054506 (2003).

[28] D. Zech, C. Rossel, L. Lesne, H. Keller, S. L. Lee, and J. Karpinski, Phys. Rev. B **54**, 12535 (1996).

[29] E. Ohmichi, E. Komatsu, T. Masui, S. Lee, S. Tajima, and T. Osada, Phys. Rev. B **70**, 174513 (2004).

[30] M. Zehetmayer, M. Eisterer, J. Jun, S. M. Kazakov, J. Karpinski, A. Wisniewski, and H. W. Weber, Phys. Rev. B **66**, 052505 (2002).

[31] V. G. Kogan, Phys. Rev. B **66**, 020509(R) (2002).